Burst and oxidation behavior of Cr-coated Zirlo during simulated LOCA testing

S. B. Bell[1,2], T. Graening[2], A. Evans[3], P. Kelly[3], B. A. Pint[2], K. A. Kane[2]
[1]Department of Materials Science and Engineering, University of Tennessee, Knoxville, TN
[2]Materials Science and Technology Division, Oak Ridge National Laboratory, Oak Ridge, TN
[3] Surface Engineering Group, Dalton Research Institute, Manchester Metropolitan University, Manchester, UK

ABSTRACT

Cr-coated Zr-alloys are a near-term cladding concept to improve reactor safety during accident scenarios. Burst and steam oxidation behavior of bare and Cr-coated Zirlo claddings were examined under simulated loss-of-coolant accident conditions. The 4.4 µm coating had no substantial effect on ballooning or opening geometry but did increase burst temperatures at higher pressures. The coating reduced steam oxidation of the cladding compared to bare specimens, but in regions of high strain, the coating developed through-cracks allowing rapid underlying zirconia formation.

INTRODUCTION

Zr claddings, historically used because of an exceptionally low thermal neutron scattering cross-section [1–3], rapidly oxidize in high temperature steam environments like those associated with station black-outs (SBO) or design basis loss-of-coolant accidents (LOCA) [4–9]. Excess oxidation heat and hydrogen gas production can exacerbate the severity of an accident, which occurred during the Fukushima Daiichi SBO. The events of 2011 accelerated the development of accident tolerant fuel (ATF) systems that aim to increase coping time in accident scenarios [2,3,10,11]. Chief among the requirements for any replacement of bare Zr claddings is reduced steam oxidation kinetics, with the aim of lowering kinetics by ≥100x [12]. Candidate cladding materials should also have similar or improved mechanical response in terms of strength, ductility, and post-failure fuel and fission product retention.

There are two possible alternatives to bare Zr claddings: (1) replacing Zr based alloys with stronger, more oxidation resistant materials like FeCrAl [2,3,13–16] or SiC-based ceramic matrix composites [17–21], or (2) application of a cladding coating to mitigate ZrO_2 formation during accident scenarios. The former is a longer-term solution, while the application of coatings is expected to be a shorter-term implementation. Thus, in recent years the community has focused its attention on Cr-coatings. Originally designed for reduction of grid-to-rod fretting [3,22], metallic Cr-coatings are resistant to high temperature steam oxidation [23–33] and hydrothermal corrosion [34–36], as well as stable under neutron irradiation [37–39].

Both transient burst testing [23,25,26,40–42] and isothermal creep burst testing [26,40] have been conducted on Cr-coated claddings with varying thicknesses and deposition methods, and generally indicate improved mechanical performance. Extensive steam oxidation testing by Brachet et al. [29,35] demonstrated the protective qualities of thinner ≤ 10 µm Cr-coatings. However, no transient burst testing has been reported detailing the impact of ≤ 10 μm coatings on cladding behavior in LOCA conditions. In this study, the effects of a 4.4 μm Cr-coating deposited with pulsed direct current (DC) magnetron sputtering on the burst behavior of Zirlo [43,44] in simulated large-break LOCA conditions was investigated. Burst strength, ballooning, and rupture geometry are presented alongside oxide analysis to assess coating performance.

EXPERIMENTAL

Details regarding simulated LOCA burst testing are reported elsewhere [15,16,45,46], but is briefly described here. Approximately 30 cm cladding segments of bare and Cr-coated Zirlo were subjected to simulated LOCA transients in a steam environment using the Severe Accident Test Station (SATS) at Oak Ridge National Laboratory (ORNL). The Cr-coatings were deposited via pulsed DC magnetron sputtering at the Advanced Materials and Surface Engineering Research Centre at Manchester Metropolitan University. Tested material was subjected to large-break LOCA conditions corresponding to limits prescribed by the U.S. Nuclear Regulatory Commission regulation 10CFR§50.46 for emergency core cooling systems. Cladding segments with alumina filler rods were internally pressurized using Ar gas and ramped from 300 to 1200 °C at a rate of 5 °C/s. The resulting burst always occurred during this ramp. After a 300 s hold at 1200 °C, the assembly was allowed to air cool to 600 °C where it was quenched in room temperature distilled water. The specimen was heated to 300°C and then steam was introduced flowing at a rate of ~30 cm/s through the quartz reaction tube, which houses the cladding train assembly. Burst pressure and temperature were recorded, and engineering hoop stress was calculated using the thin-walled approximation for hoop stress,

$$\sigma_H = \frac{PR}{h}, \qquad \text{Eq. 1}$$

where σ_H is the burst hoop stress (MPa), P is the burst internal overpressure (MPa), R is the pre-transient mean radius (mm), and h is the initial thickness of the cladding wall (mm). Cladding geometry was measured with digital calipers and is reported in Table 1. To account for uncertainty in burst temperatures, half of the difference between the two thermocouple readings that were closest to the rupture was used as error bars.

After burst, a Keyence VR-3100 microscope was used to image the full length of the claddings [16]. Burst opening area and length (from end to end of the rupture) were measured via image analysis. Diametric strain profiles were generated using caliper measurements along the axial direction. Metallographic cross-sections were taken from the base of the claddings before testing to assess the initial coating thickness and microstructure as well as after burst from regions of approximately largest deformation. Scanning electron microscopy (SEM), including back-scatter electron (BSE) imaging and energy dispersive X-ray spectroscopy (EDS), was performed using a Tescan model MIRA3 at an operating voltage of 10 kV. ImageJ software was used to measure wall and oxide thickness along the cladding cross-sections after testing from stitched optical macrographs. To determine the thickness of the as-received coating and post-testing reaction layers, the publicly available Size of Oxidation Feature from Image Analysis (SOFIA) software [47,48] was used on higher magnification SEM micrographs. A micrograph showing a cross-section from a coated sample prior to testing is presented in Figure 1. The coating was well adhered with no through-cracking, although limited cracking was observed at the coating-cladding interface. Coating thickness was found to be 4.40 ± 0.24 µm.

RESULTS

Burst strength characterization

The relationship between both burst hoop stress and burst pressure with temperature is reported in Figure 2(a) and (b), respectively, as well as in Table 2. Bare Zirlo is shown in orange squares and the Cr-coated samples in purple diamonds. Data (green dashed line) from previous burst testing of C26M FeCrAl [16] and an empirical model [49,50] for Zircaloys with a 5 °C/s heating rate (grey line) are included as references. At an initial pressure of ~1 MPa, the Cr-coated sample burst at a temperature 36 °C lower than the respective bare cladding but at ~3.4 MPa and ~5.9 MPa, the Cr-coated Zirlo withstood 32°C and 42 °C greater temperatures, respectively, than the bare cladding.

Ballooning and deformation

Optical images of claddings that were initially pressurized to ~1 MPa, ~3.4 MPa, and ~5.9 MPa are shown after burst in Figure 3. The bare samples are shown in Figure 3(a), (c), and (e) and the Cr-coated samples in Figure 3(b), (d), and (f). Visually, there is no clear difference in the ballooning profiles between the coated and bare samples at the same initial pressure. To quantitatively assess differences in ballooning, diametric strain profiles for claddings that had initial pressures of ~1 MPa and ~3.4 MPa are reported in Figure 4(a) and (b), respectively. For the same initial internal pressures, the strain profiles reached comparable maximum diametric strain values and displayed similar profile form. Analogous results were found for the diametric strain of ~5.9 MPa initial pressure samples. In the limited testing presently performed, the 4.4 µm Cr-coating had no apparent impact on decreasing ballooning during LOCA burst testing. The small drops on either side of the large peaks in Figure 4(a) and (b) are due to constriction from the Pt-Rh wire securing the thermocouples.

Opening geometry analysis

Figure 5 shows higher magnification optical images of the burst regions for the ~3.4 and ~5.9 MPa initial pressure samples, with the bare claddings shown in Figure 5(a) and (b). The bare samples exhibited lenticular openings and the Cr-coated claddings, Figure 5(c) and (d), had a similar opening shape, but with cracking observed near the ends of the ruptures for all samples. Burst opening area and length versus hoop stress are reported in Figure 6. Generally, the bare and Cr-coated samples exhibited comparable opening areas and lengths. The ~3.4 MPa initial pressure Cr-coated sample demonstrated a larger opening area and length than the respective bare sample, while the ~5.9 MPa Cr-coated cladding exhibited a smaller area and length than the corresponding bare cladding. The ~1 MPa initial pressure bare Zirlo sample, Figure 3(a), broke during handling and is not reported.

Oxidation analysis of regions opposite from burst

Cross sections were taken from the ~1 MPa initial pressure bare and Cr-coated Zirlo claddings from regions of approximately largest deformation. Optical micrographs of the subsequent entire specimen mounts are shown in Figure 7(a) and (c). The Cr-coated cladding,

Figure 7(c), cracked during post-test handling and mounting. For both bare and coated Zirlo, the cladding wall thickness decreased significantly at the burst tips, indicating high amounts of strain, while in the regions positioned ~180° from burst, wall thinning was considerably less. Higher magnification micrographs centered in the regions ~180° from burst are shown in Figure 7(b) and (d). For the bare cladding, extensive ZrO_2 formation occurred on both the inner diameter (ID) and outer diameter (OD), 57.3 ± 6.8 and 37.4 ± 1.4 µm thick, respectively. For the coated sample, Figure 7(d), ZrO_2 formation was mitigated entirely on the OD in regions ~180° from burst.

A higher magnification BSE micrograph of the ~ 1 MPa initial pressure Cr-coated sample (Figure 7) is shown in Figure 8(a). A Cr_2O_3 layer is present on the ambient surface of the cladding, with a residual Cr layer underneath. Between the residual Cr-coating and the Zr substrate, a Zr-Cr interdiffusion zone (IDZ) formed. An EDS line scan through all three reaction layers is reported in Figure 8 (b). Figure 9(a) and (b) report more detailed statistics using box and whisker plots of the formed reaction layers for the coated and bare samples, respectively. The Cr_2O_3, residual Cr, and Zr-Cr IDZ layers had thicknesses of 0.94 ± 0.15 µm, 2.90 ± 0.18 µm, and 0.81 ± 0.20 µm, respectively.

Oxidation analysis of regions of high strain

Oxidation behavior of the Cr-coated cladding in regions of high strain closer to the burst opening differed from regions ~180° from the burst. Figure 10(a) presents a stitched optical macrograph of the burst tip for a Cr-coated sample (~1 MPa initial pressure), showing that in regions of higher strain, the Cr-coating did not mitigate ZrO_2 formation. Large amounts of ZrO_2 were present towards the opening, ~50-60 µm thick on both the OD and ID near the burst tips. OD ZrO_2 formation tapered off as distance away from the burst tip increases, until eventually none was formed and the structure in Figure 8 is found.

To quantify the association of oxide formation with strain, residual wall and ZrO_2 layer thickness measurements were made along the Cr-coated cross-section in Figure 7. "Wall-strain" was then calculated using the equation,

$$\varepsilon_{wall} = \frac{h-h_0}{h_0}, \qquad \text{Eq. 2}$$

where ε_{wall} is wall-strain, h is the unconsumed metallic wall-thickness after testing, and h_0 is the pre-transient wall-thickness. As most of the ZrO_2 formation occurred during the 300 s hold at 1200 °C after burst, metal consumption was corrected for using OD and ID oxide thicknesses and the Pilling-Bedworth ratio [51]. Metal consumption was then added to measurements of the unconsumed wall-thickness, as this corrected value is more representative of wall-thickness along the cross-section immediately after burst. The unconsumed wall-strain (blue triangles), the corrected wall-strain (purple diamonds), and the OD oxide thickness (grey squares) along the Cr-coated cross-section (Figure 7) are reported in Figure 10(b).

The burst tips are represented as 0 and 1 fractional distance in Figure 10(b). Opposite the burst opening, $|\varepsilon_{wall}|$ reached a minimum and no ZrO_2 was detected on the coated OD. ZrO_2 formation began on either side of this minimum, starting where $|\varepsilon_{wall}|$ reached ~15%. Moving towards the burst region, both the $|\varepsilon_{wall}|$ and OD ZrO_2 thickness increased to maximum values near the opening, demonstrating a relationship between the two.

To investigate coating behavior near the burst region, higher magnification BSE micrographs along with EDS elemental maps of Cr, Zr, and O were generated, Figure 11. Figure 11(a) reveals two distinct structures in areas near the burst: (1) regions of partially consumed coating and (2) regions of fully consumed coating. In areas of fully consumed Cr, large through-cracking formed in the Cr_2O_3 layer, coinciding with a thicker underlying ZrO_2 scale. Figure 11(b) shows a higher magnification micrograph centered on a region of partially consumed Cr. A crack through the residual Cr-coating connecting the Cr_2O_3 and underlying ZrO_2 formation can clearly be seen. EDS maps shown in Figure 11(c), (d), and (e) reveal the presence of O and Zr in the through-crack, while Cr is absent. In regions of intermediate wall-strain, between the area ~180° from the rupture and the burst tips, areas of accelerated localized corrosion were found on the OD, seen in Figure 12, indicating the coating failed but to a lesser degree.

DISCUSSION

Burst behavior

Due to material constraints, the necessary replicate testing was not performed to definitively assess observed differences in behavior. Considering this, a range of initial pressures were selected to preliminarily compare burst behavior. At higher burst pressures/stresses, a 4.4 µm Cr-coating increased burst temperatures compared to bare Zirlo, Figure 2. However, the lower initial pressure coated sample, ~1 MPa, exhibited a lower burst temperature. These findings are reasonably consistent with preliminary results from Brachet et al.'s [26] ramp testing of M5 claddings with 10-15 µm coatings, where comparable or slightly higher burst temperatures were observed.

In terms of deformation, both maximum diametric strain as well as the ballooning shape of the profiles, Figure 4, were similar between the bare and Cr-coated samples. Opening geometry, Figure 6, was also not affected by the coating. The lack of reduction to diametric strain and similar opening geometry does not align with previous ramp testing [23,25,26,41] of thicker coatings, where significant reduction in ballooning and rupture size was observed. For Zirlo, there may be a thickness threshold above 4.4 µm where Cr-coatings provide a benefit of reduced deformation and opening size.

For the coated samples, cracking was observed near the ends of the burst openings, Figure 5. There may be a distinct shift from a regime of ductile fracture near the center of the openings to brittle fracture at the ends. It is possible that these cracks formed during the quench at 600 °C, long after burst, due to thermally induced stresses. While the standard LOCA test is used to evaluate coating performance, the 1200°C hold and quench greatly complicate analysis of the coating when burst occurred. It might be more useful to stop the test immediately after burst and cool the specimen.

Reaction product formation in regions of complete mitigation

Previous studies [28–31] on Cr-coated Zr systems in 1200 °C steam environments and considerations of the Zr-Cr phase diagram [52] suggest the IDZ most likely consists of a $ZrCr_2$ intermetallic. Pores were observed at the Zr-IDZ interface as well as the Cr-Cr_2O_3 interface, Figure 8(a). Hu et al. [28] found large voids in the Zr substrate at the Zr-IDZ interface that were related to Cr and Sn segregation. Brachet et al. [29] suggested that the pores are Kirkendall voids, with the cavities at the Cr-Cr_2O_3 interface resulting from outward cationic diffusion [53], while cavities at the Zr-IDZ boundary result from vacancy flux due to differences in solubility and diffusivity between the Cr-coating and Zirlo substrate.

Oxidation near and away from the burst region

As expected, the Cr-coating reduced ZrO_2 formation compared to bare cladding, with complete mitigation in regions away from the burst during the simulated LOCA, Figure 7(d) and Figure 10(b). However, the presence of ZrO_2 indicates coating failure along much of the OD, where for ~1/2 of the cladding cross-section ZrO_2 formation was ≥10 μm. The coating integrity was compromised in regions of higher strain, demonstrated by the development of cracks and extensive ZrO_2 formation, Figure 11(b), which were not present in regions ~180° from opening, Figure 8. As through-coating cracking was not observed in the as-received condition, Figure 1, ballooning and burst likely caused these developments. It is possible that these newly formed cracks provided a short-circuit pathway for oxidants to the underlying Zr cladding evidenced by EDS maps, Figure 11, leading to increased ZrO_2 formation and potential consumption of the Cr-coat from both interfaces.

The observed relationship between OD ZrO_2 thickness and wall-strain, Figure 10(b), indicates that where $|\varepsilon_{wall}| \geq$ ~15 %, the Cr-coating failed under these conditions. Observation of the oxide in intermediate wall-strain regions, Figure 12, revealed localized formation of ZrO_2. The structure of these localized corrosion areas resembles the "nodular ZrO_2 spots" reported by Brachet et al. [35] during steam oxidation testing of coated Zircaloy-4 samples with pre-cracking. It is possible that regions of higher strain formed more cracks. With more short-circuit pathways, local oxidation rates would be higher. This could explain the association of wall-strain and ZrO_2 thickness. The "wall-strain" presented in this study is not a typical measurement associated with the stress state in thin-walled tube geometry and is intended as a proxy for other more rigorous valuations such as axial, radial, or hoop strain during deformation. As such, the correlation of strain with coating failure where $|\varepsilon_{wall}| \geq$ ~15 % is only for wall-strain, and the possible effects of strain-rate are not represented. Also, the wall-strain along the circumference was non-uniform, evidenced by the asymmetric deformation shown on either side of the minimum in Figure 10(b). Non-uniform strain/strain rate could influence coating failure.

While there was only partial protection in regions of high wall-strain, the coating still reduced or prevented Zr oxidation for the entirety of the cladding. Therefore a 4.4 μm Cr-coating demonstrated improvements in reducing steam oxidation relative to bare claddings during simulated LOCA conditions. However, a more complete study of the critical Cr-coating thickness is needed to determine statistically significant improvements in burst behavior, such that the optimum coating thickness can be evaluated based on a cost-benefit analysis of both normal operating and accident condition performance.

CONCLUSIONS

Simulated LOCA burst testing at a heating rate of 5 °C/s was performed on Cr-coated and bare Zirlo cladding segments. A 4.4 μm thick Cr-coating deposited by pulsed DC magnetron sputtering provided some improvement in burst temperatures at higher internal stresses, but no discernable effect on ballooning behavior and opening geometry was observed. For most of the cladding circumference, the Cr-coated Zirlo reduced underlying oxide formation on the cladding outer surface. However, in regions of high wall-strain, $|\varepsilon_{wall}| \geq$ ~15 %, which accounted for ~1/2 of the cladding cross-section, the coating developed cracks that contributed to ZrO_2 formation by providing short-circuit diffusion pathways.

ACKNOWLEDGEMENTS

The authors would like to thank B. Johnston for conducting the burst testing presented in this study, as well as M. Ridley and B. Garrison for technical review. This work was performed as a part of the Advanced Fuels Campaign directed by the United States Department of Energy Office of Nuclear Energy. The study was part-funded under the £46m Advanced Fuel Cycle Programme as part of the Department for Business, Energy and Industrial Strategy’s (BEIS) £505m Energy Innovation Programme. The authors would also like to thank Westinghouse Electric Sweden AB for providing samples of Zirlo tubing for testing.

TABLES

Table 1. Pre-transient geometry of the bare and coated Zirlo claddings.

Cladding Material	Inner radius (mm)	Mean radius (mm)	Wall-thickness (mm)
Zirlo	4.135	4.440	0.610
Cr-coated Zirlo (4.4 µm)	4.135	4.442	0.614

Table 2. Burst temperature, pressure, and hoop stress for all tests conducted in this study.

Cladding Material	Burst temperature (°C)	Burst hoop stress (MPa)	Burst pressure (MPa)
Zirlo	747	57.4	7.88
	766	49.1	6.74
	835	25.4	3.49
	977	6.76	0.929
Cr-coated Zirlo (4.4 µm)	808	48.3	6.69
	867	28.0	3.87
	941	7.54	1.04

FIGURES

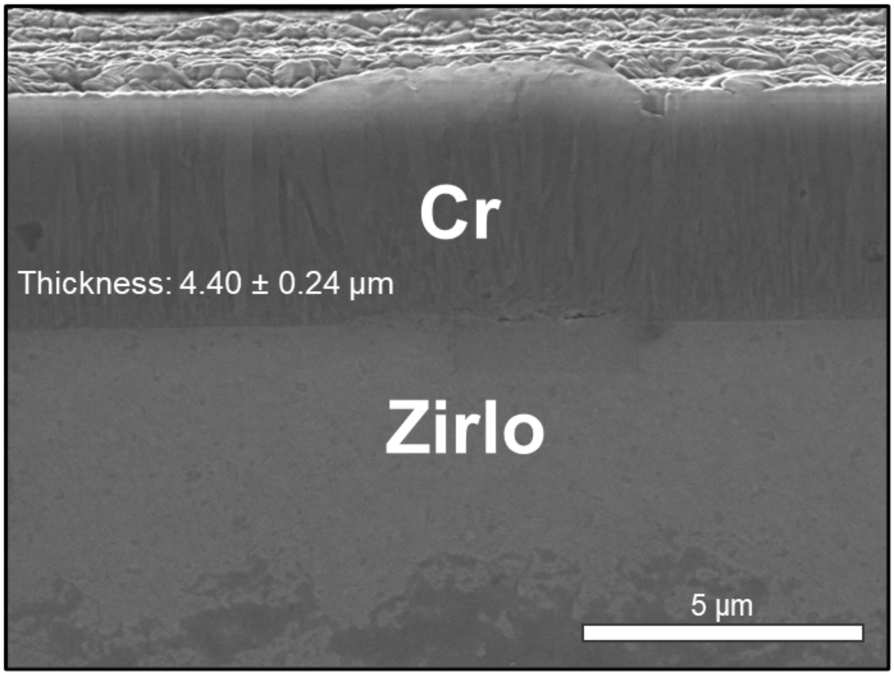

Figure 1. SEM micrograph of a cross-section from the base of a Cr-coated Zirlo cladding prior to testing.

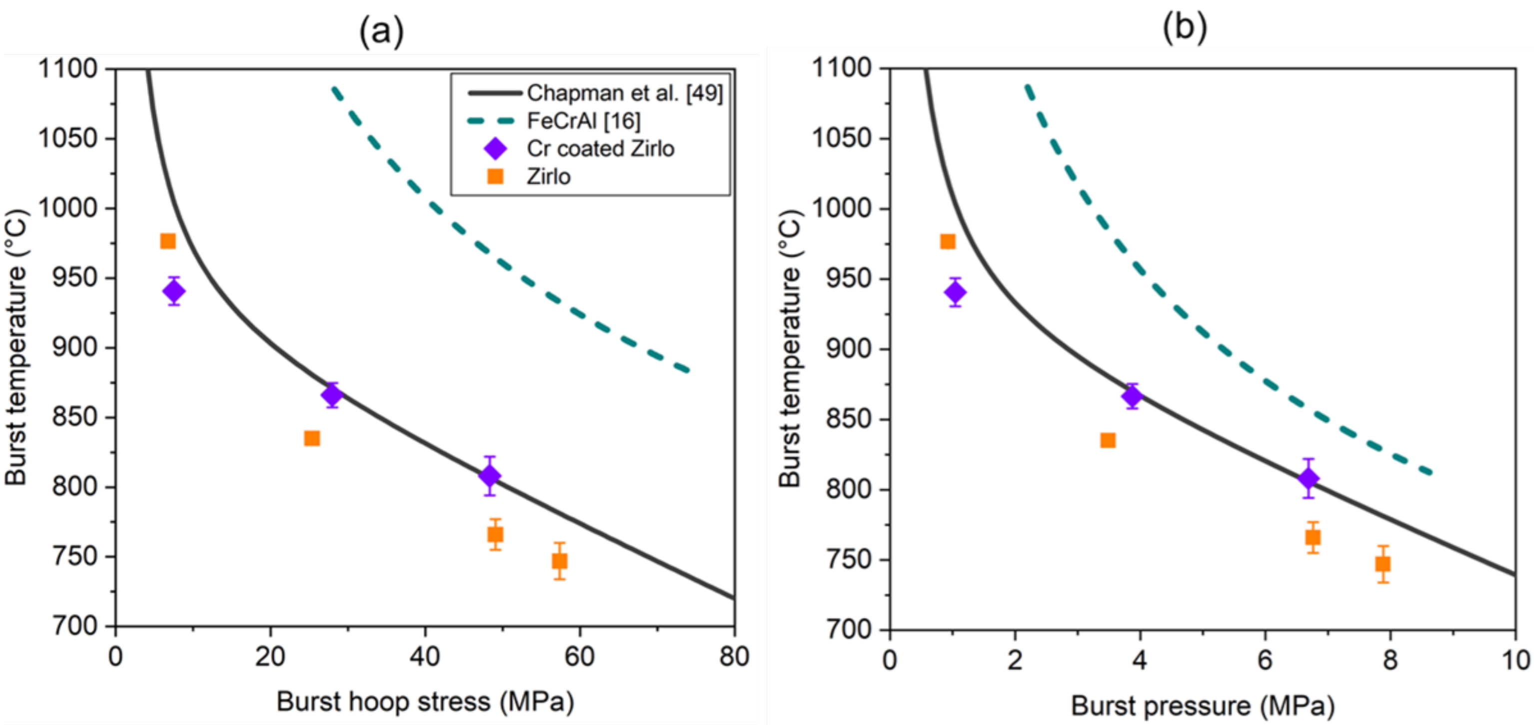

Figure 2. Relationship between temperature and (a) hoop stress and (b) burst pressure for bare Zirlo (orange squares) and Cr-coated Zirlo (purple diamonds). The trendline for C26M FeCrAl [16], green dashed line, and the Chapman et al. correlation line for Zircaloys [49,50], grey line, are included as references. The Chapman correlation line for hoop stress in (a) was converted to burst pressure in (b) using the bare Zirlo pre-transient geometry, Table 1.

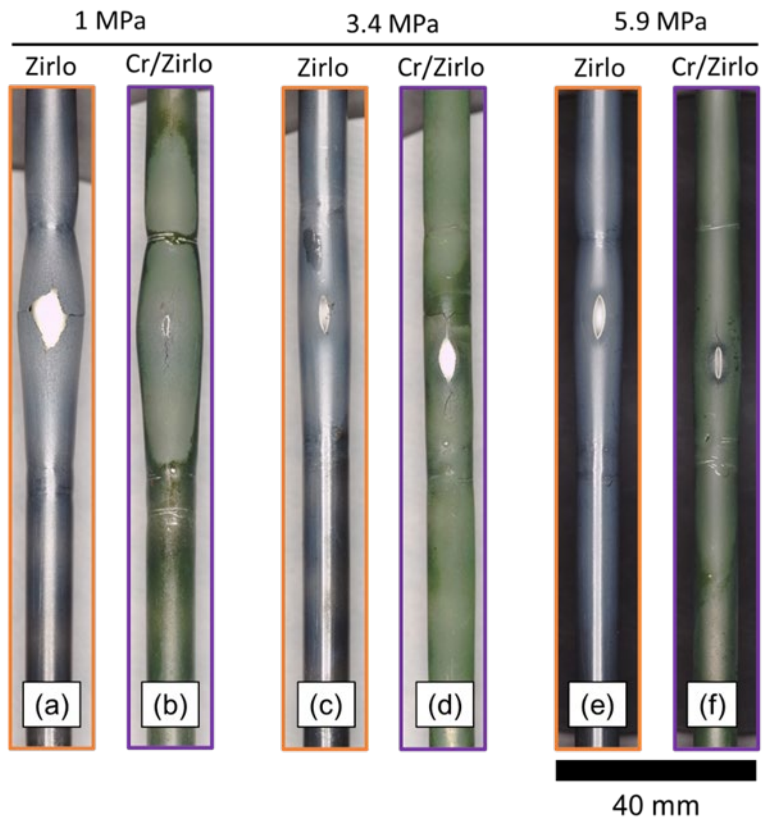

Figure 3. Optical macrographs of burst Zirlo and Cr-coated Zirlo at initial pressures of (a,b) 1 MPa, (c,d) 3.4 MPa, and (e,f) 5.9 MPa. The 1 MPa initial pressure bare Zirlo sample has significantly larger opening than the comparable Cr-coated sample. The large opening in (a) formed during post-test handling due to severe embrittlement of the cladding.

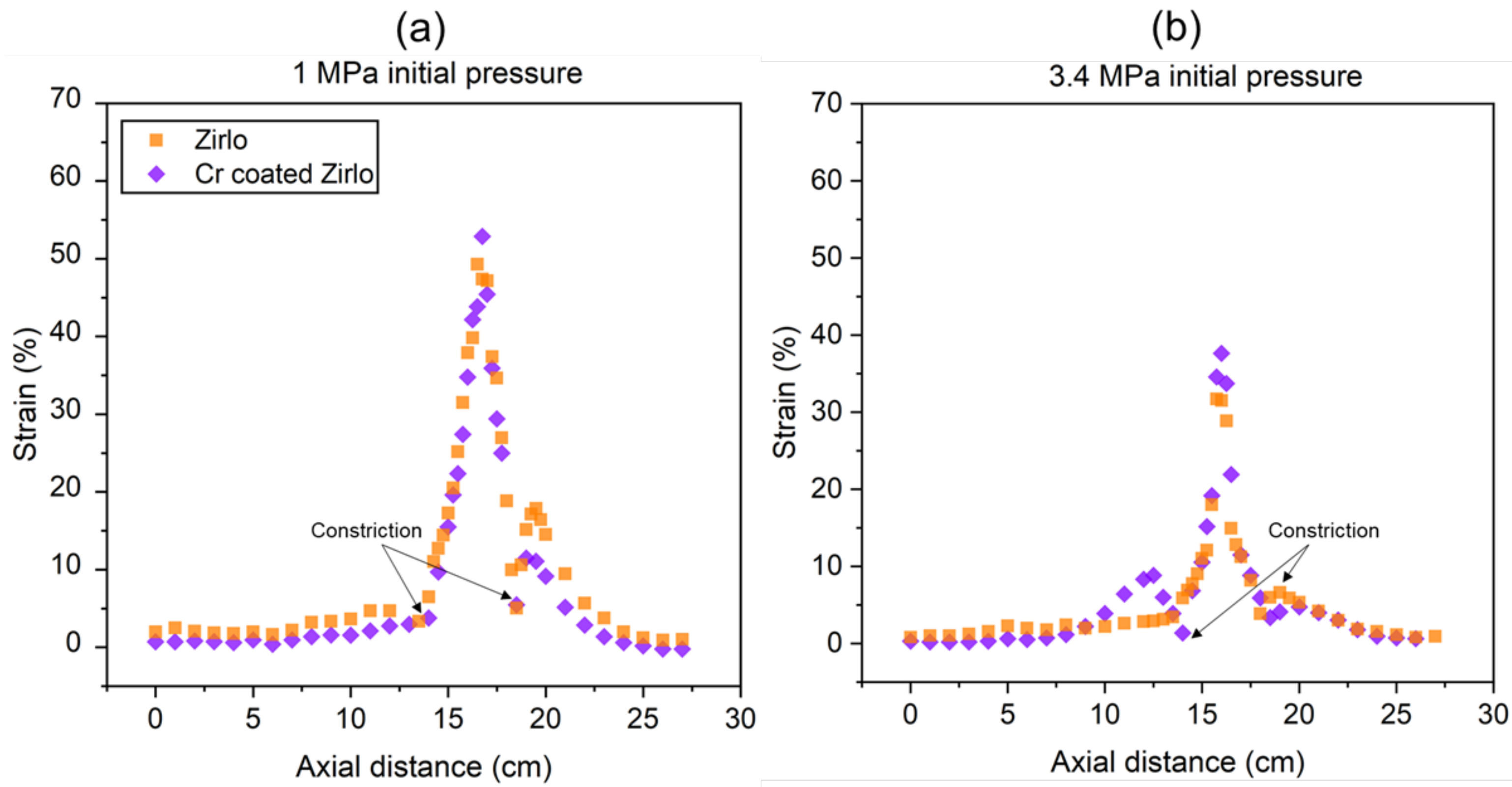

Figure 4. Post-burst diametrical strain measurements along cladding axial distance for Zirlo (orange squares) and Cr-coated Zirlo (purple diamonds) at initial pressures of (a) ~1 MPa and (b) ~3.4 MPa. The black arrows indicate the axial location where constriction from the Pt-Rh wire that secured the thermocouples occurred.

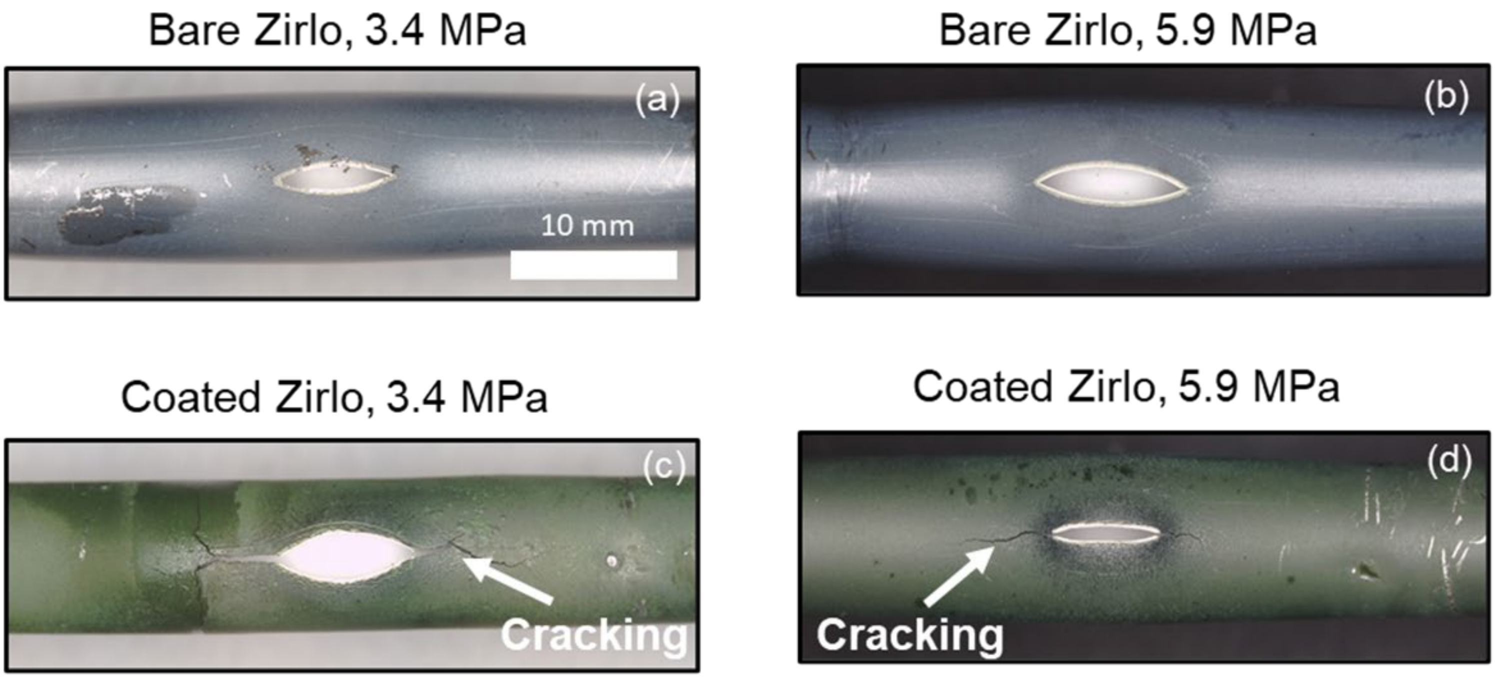

Figure 5. Higher magnification optical images of the burst regions for claddings that had ~3.4 and ~5.9 MPa initial pressures. The bare samples are shown in (a) and (b), the Cr-coated samples are shown in (c) and (d).

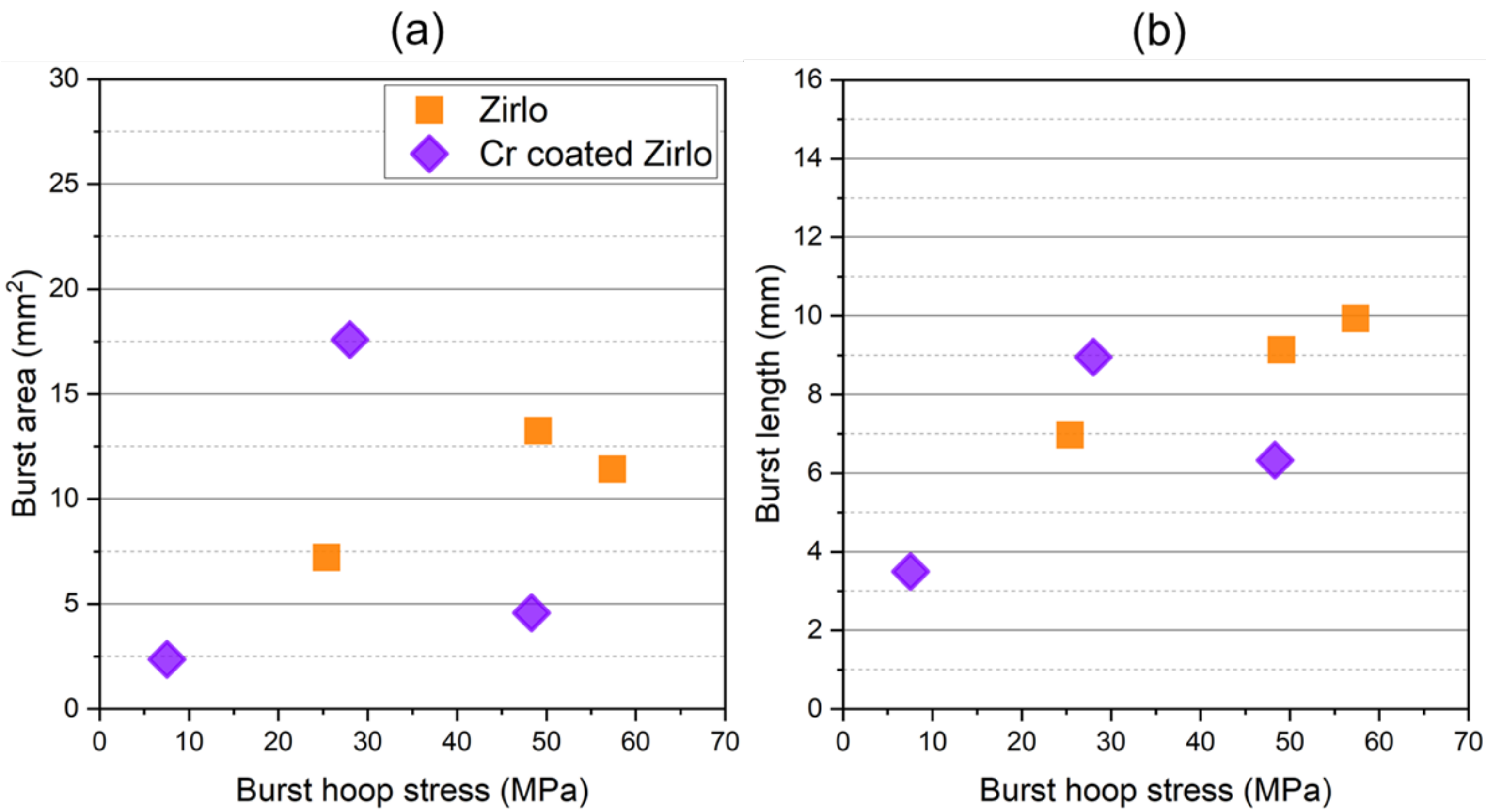

Figure 6. (a) Burst opening area and (b) burst opening length versus hoop stress for Cr-coated and bare Zirlo.

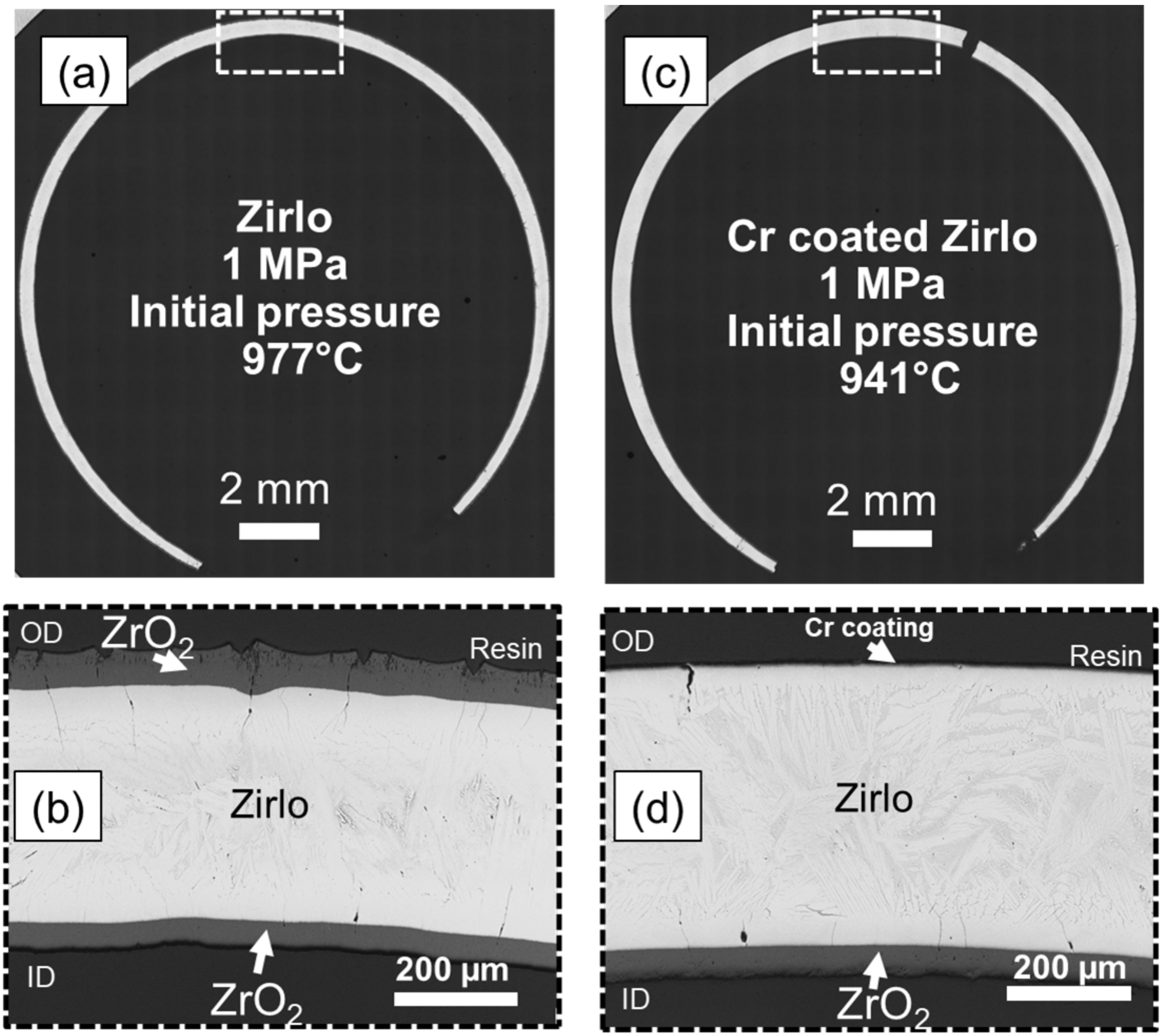

Figure 7. Cross-sectional optical macrograph taken from the burst region of Zirlo (1 MPa initial pressure) and (b) higher magnification micrograph of region opposite burst opening, indicated by dashed box. (c) Similar macrograph taken from burst region of Cr-coated Zirlo (1 MPa initial pressure) and (d) higher magnification micrograph taken from region opposite burst, also indicated by dashed box.

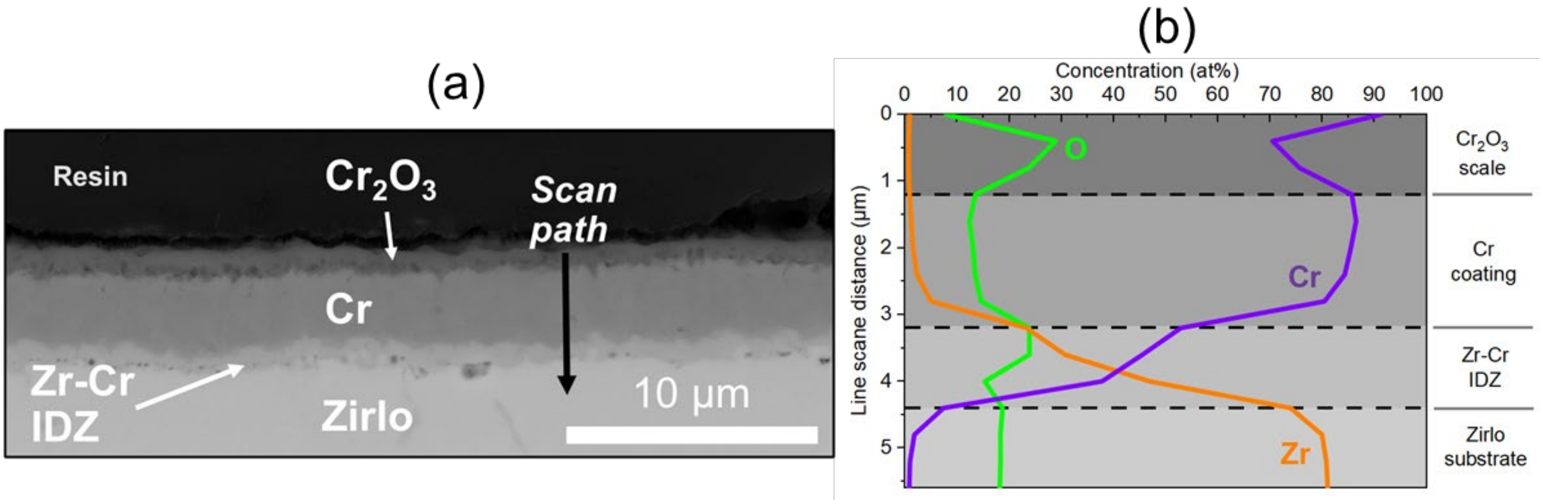

Figure 8. Representative BSE micrograph of the Cr-Zirlo interface taken in a region opposite burst (1 MPa initial pressure). (b) EDS line scan across the reaction layers.

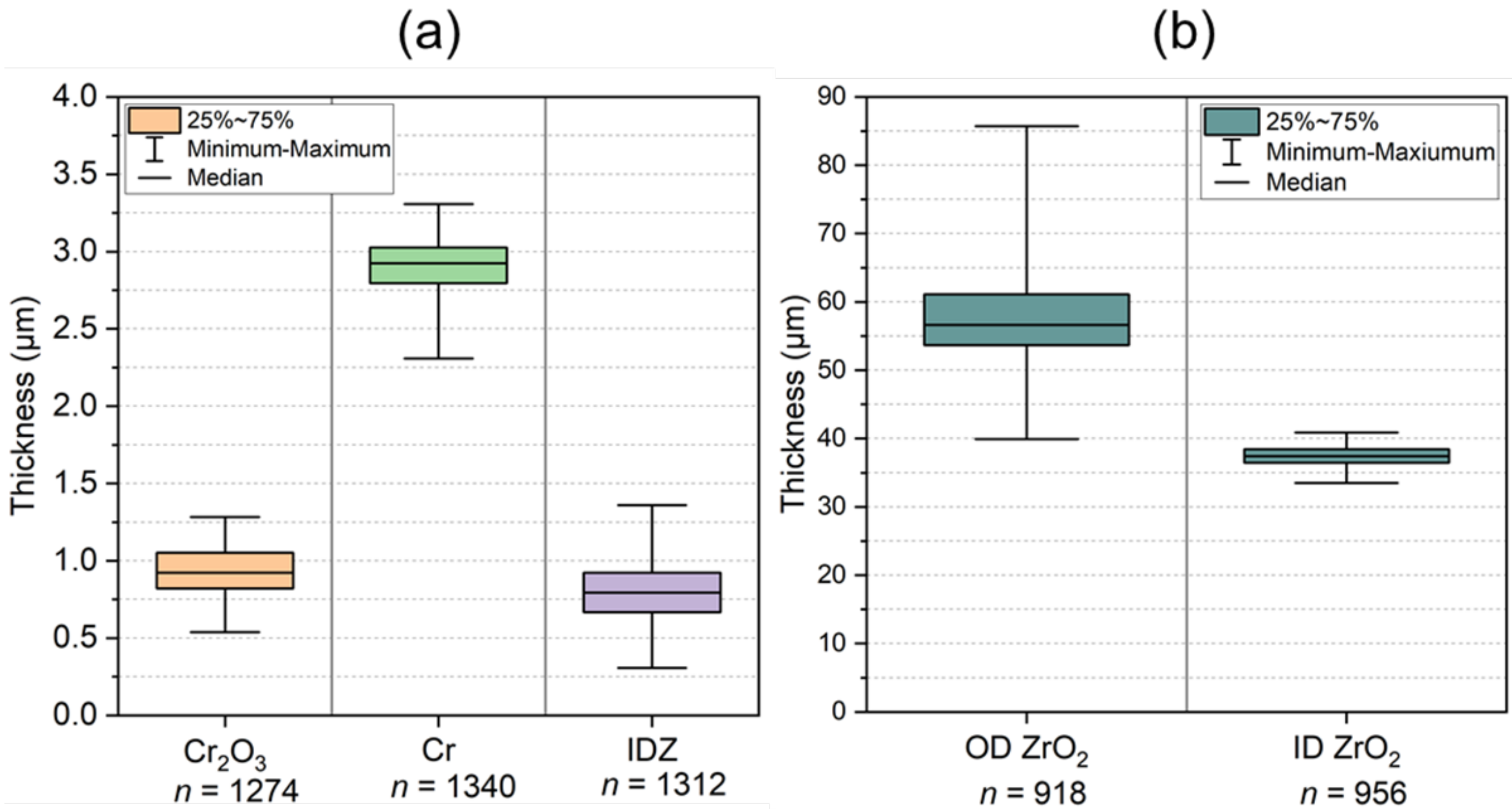

Figure 9. (a) Thickness data of reaction layers shown in Figure 8 and (b) oxide scale thickness data from the micrograph in Figure 7(b). "n" represents the number of measurements.

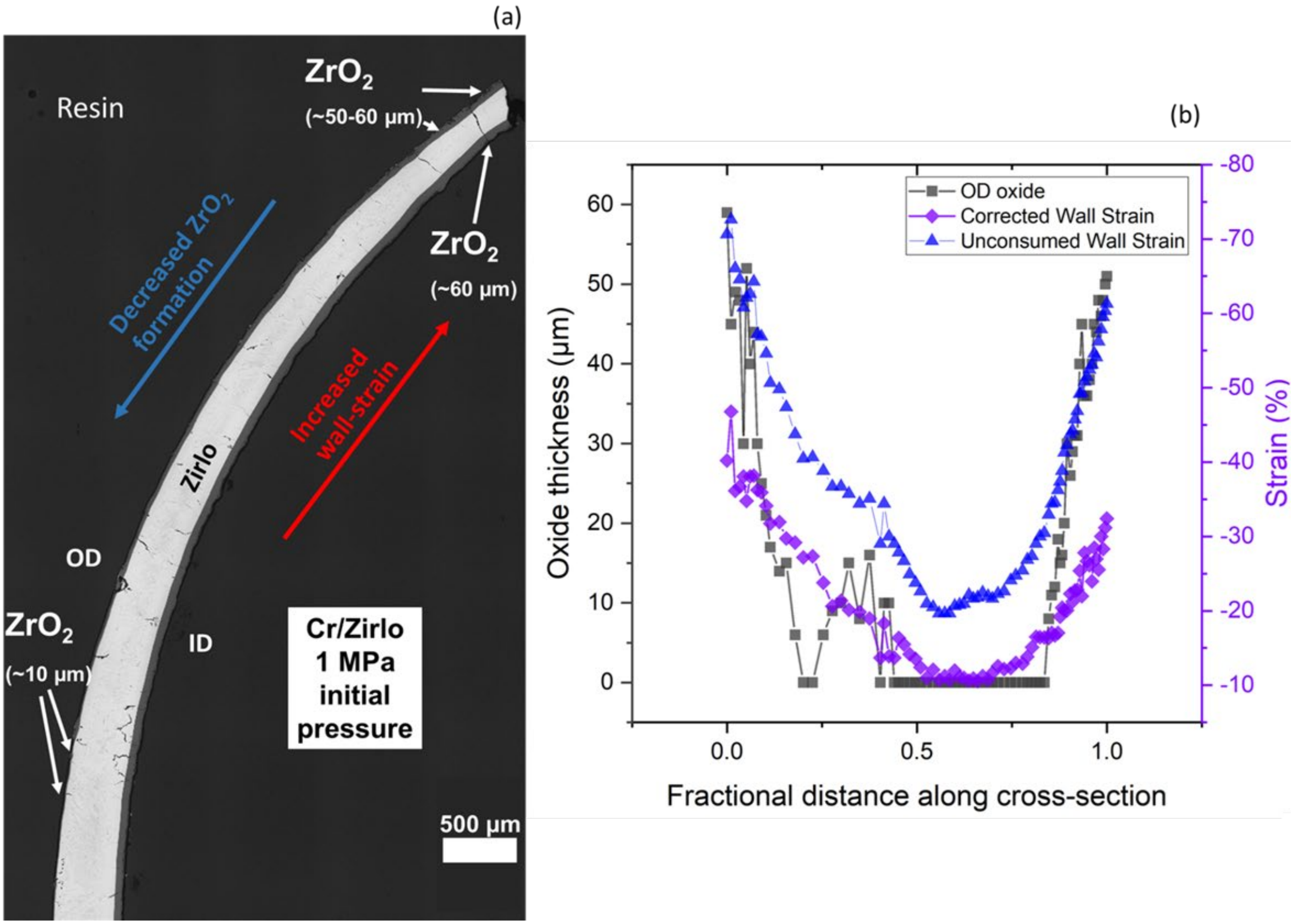

Figure 10. (a) Optical macrograph of the burst tip of a Cr-coated Zirlo sample (1 MPa initial pressure) showing the tapering of zirconia formation away from the burst region. (b) OD oxide thickness and wall-strain versus fractional distance along the cross-section in Figure 7(c). 0 and 1 fractional distance represent either end of the cross-section, i.e., the burst tips. Unconsumed wall-strain values, blue triangles, were calculated using the residual metal thickness after oxidation/testing. Corrected wall-strain

values, purple diamonds, were calculated by adding the thickness of metal lost due to oxidation to the unconsumed metal thickness. Metal consumption was determined using the Pilling-Bedworth ratio [51].

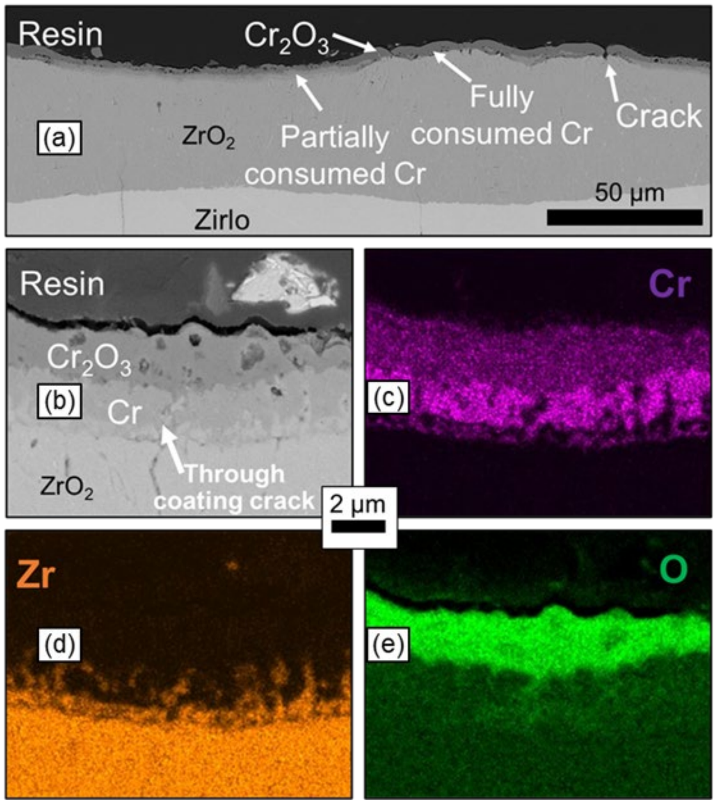

Figure 11. (a) BSE micrograph of the oxide scales that form in the burst tip vicinity. (b) Higher magnification BSE micrograph representative of regions where the Cr-coating was partially consumed, and associated (C) Cr, (d) Zr, and (e) O elemental maps.

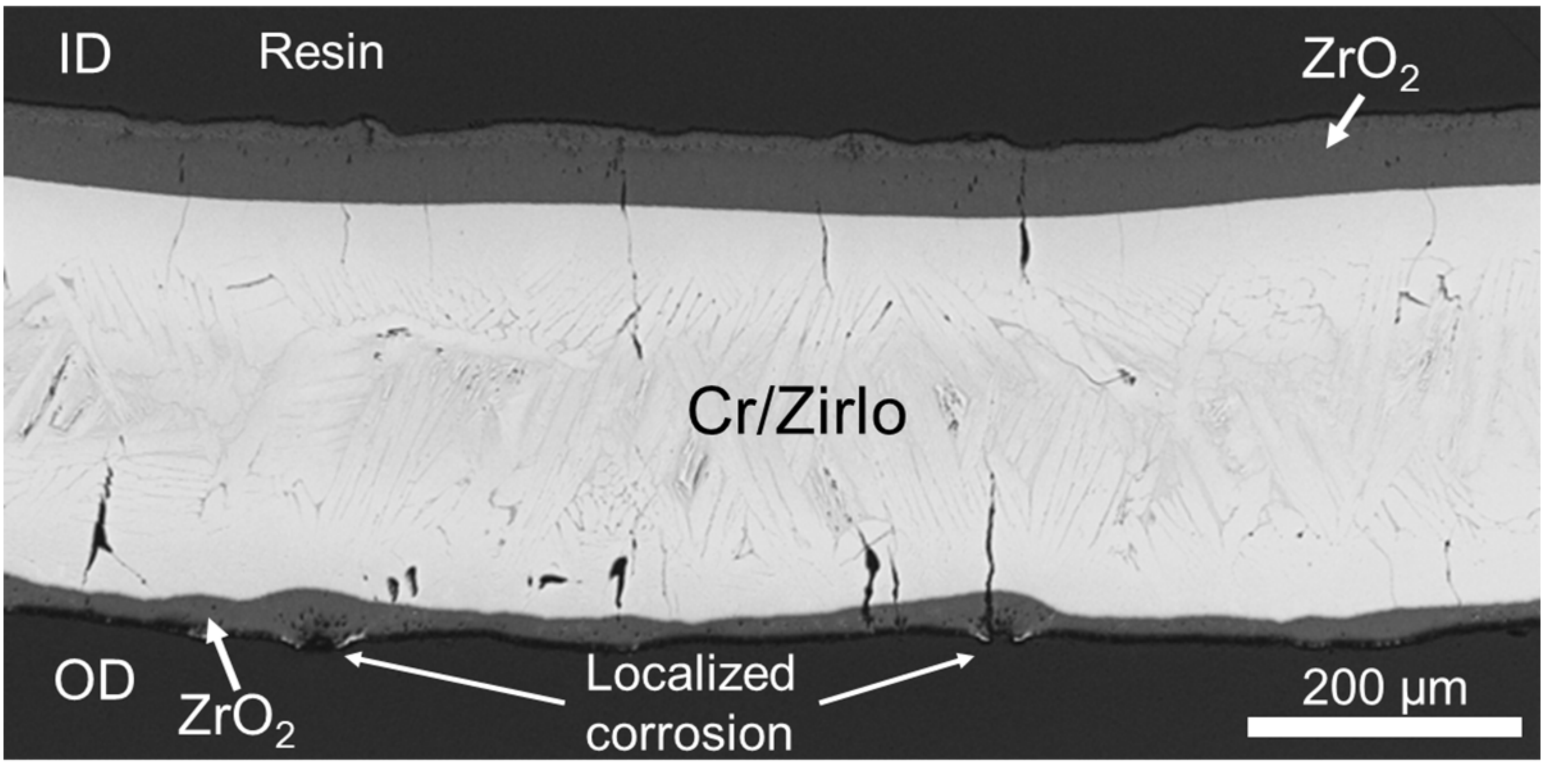

Figure 12. Higher magnification micrograph of a region of intermediate wall-strain, illustrating the areas of localized corrosion.

REFERENCES

[1] S.J. Zinkle, G.S. Was, Materials challenges in nuclear energy, Acta Mater. 61 (2013) 735–758. https://doi.org/10.1016/j.actamat.2012.11.004.

[2] R.B. Rebak, Alloy Selection for Accident Tolerant Fuel Cladding in Commercial Light Water Reactors, Metall. Mater. Trans. E. 2 (2015) 197–207. https://doi.org/10.1007/s40553-015-0057-6.

[3] K.A. Terrani, Accident tolerant fuel cladding development: Promise, status, and challenges, J. Nucl. Mater. 501 (2018) 13–30. https://doi.org/10.1016/j.jnucmat.2017.12.043.

[4] V.F. Urbanic, T.R. Heidrick, High-temperature oxidation of Zircaloy-2 and Zircaloy-4 in steam, J. Nucl. Mater. 75 (1978) 251–261.

[5] S. Kawasaki, T. Furuta, M. Suzuki, Oxidation of Zircaloy-4 under High Temperature Steam Atmosphere and Its Effect on Ductility of Cladding, J. Nucl. Sci. Technol. 15 (1978) 589–596. https://doi.org/10.1080/18811248.1978.9735555.

[6] R.E. Pawel, J.V. Cathcart, R.A. McKee, The Kinetics of Oxidation of Zircaloy-4 in Steam at High Temperatures, J. Electrochem. Soc. 126 (1979) 1105–1111.

[7] S. Leistikow, S.G. Schanz, The oxidation behavior of Zircaloy-4 in steam between 600 and 1600°C, Mater. Corros. Korros. 36 (1985) 105–116. https://doi.org/10.1002/maco.19850360302.

[8] S. Leistikow, G. Schanz, Oxidation kinetics and related phenomena of zircaloy-4 fuel cladding exposed to high temperature steam and hydrogen-steam mixtures under PWR accident conditions, Nucl. Eng. Des. 103 (1987) 65–84. https://doi.org/10.1016/0029-5493(87)90286-X.

[9] M. Steinbrück, N. Vér, M. Große, Oxidation of Advanced Zirconium Cladding Alloys in Steam at Temperatures in the Range of 600–1200 °C, Oxid. Met. 76 (2011) 215–232. https://doi.org/10.1007/s11085-011-9249-3.

[10] L.J. Ott, K.R. Robb, D. Wang, Preliminary assessment of accident-tolerant fuels on LWR performance during normal operation and under DB and BDB accident conditions, J. Nucl. Mater. 448 (2014) 520–533. https://doi.org/10.1016/j.jnucmat.2013.09.052.

[11] S.J. Zinkle, K.A. Terrani, J.C. Gehin, L.J. Ott, L.L. Snead, Accident tolerant fuels for LWRs: A perspective, J. Nucl. Mater. 448 (2014) 374–379. https://doi.org/10.1016/j.jnucmat.2013.12.005.

[12] B.A. Pint, K.A. Terrani, Y. Yamamoto, L.L. Snead, Material Selection for Accident Tolerant Fuel Cladding, Metall. Mater. Trans. E. 2 (2015) 190–196. https://doi.org/10.1007/s40553-015-0056-7.

[13] B.A. Pint, K.A. Terrani, M.P. Brady, T. Cheng, J.R. Keiser, High temperature oxidation of fuel cladding candidate materials in steam–hydrogen environments, J. Nucl. Mater. 440 (2013) 420–427. https://doi.org/10.1016/j.jnucmat.2013.05.047.

[14] Y. Yamamoto, B.A. Pint, K.A. Terrani, K.G. Field, Y. Yang, L.L. Snead, Development and property evaluation of nuclear grade wrought FeCrAl fuel cladding for light water reactors, J. Nucl. Mater. 467 (2015) 703–716. https://doi.org/10.1016/j.jnucmat.2015.10.019.

[15] K.A. Kane, S.K. Lee, S.B. Bell, N.R. Brown, B.A. Pint, Burst behavior of nuclear grade FeCrAl and Zircaloy-2 fuel cladding under simulated cyclic dryout conditions, J. Nucl. Mater. 539 (2020) 152256. https://doi.org/10.1016/j.jnucmat.2020.152256.

[16] S.B. Bell, K.A. Kane, C.P. Massey, L.A. Baldesberger, D. Lutz, B.A. Pint, Strength and rupture geometry of un-irradiated C26M FeCrAl under LOCA burst testing conditions, J. Nucl. Mater. 557 (2021) 153242. https://doi.org/10.1016/j.jnucmat.2021.153242.

[17] Y. Katoh, L.L. Snead, C.H. Henager, T. Nozawa, T. Hinoki, A. Iveković, S. Novak, S.M. Gonzalez de Vicente, Current status and recent research achievements in SiC/SiC composites, J. Nucl. Mater. 455 (2014) 387–397. https://doi.org/10.1016/j.jnucmat.2014.06.003.

[18] V. Angelici Avincola, M. Grosse, U. Stegmaier, M. Steinbrueck, H.J. Seifert, Oxidation at high temperatures in steam atmosphere and quench of silicon carbide composites for nuclear application, Nucl. Eng. Des. 295 (2015) 468–478. https://doi.org/10.1016/j.nucengdes.2015.10.002.

[19] Y. Katoh, L.L. Snead, Silicon carbide and its composites for nuclear applications – Historical overview, J. Nucl. Mater. 526 (2019) 151849. https://doi.org/10.1016/j.jnucmat.2019.151849.

[20] H. Kishimoto, J.-S. Park, N. Nakazato, A. Kohyama, Silicon Dissolution and Morphology Modification of NITE SiC/SiC Claddings in Pressurized Flowing Water under Neutron Irradiation, J. Nucl. Mater. (2021) 153253. https://doi.org/10.1016/j.jnucmat.2021.153253.

[21] T. Koyanagi, H. Wang, J.D.A. Mena, C.M. Petrie, C.P. Deck, W.-J. Kim, D. Kim, C. Sauder, J. Braun, Y. Katoh, Thermal diffusivity and thermal conductivity of SiC composite tubes: the effects of microstructure and irradiation, J. Nucl. Mater. 557 (2021) 153217. https://doi.org/10.1016/j.jnucmat.2021.153217.

[22] W.J. Bryan, D. Jones, Wear resistant coating for fuel cladding, US5268946A, 1993.

[23] H.-G. Kim, I.-H. Kim, Y.-I. Jung, D.-J. Park, J.-Y. Park, Y.-H. Koo, Adhesion property and high-temperature oxidation behavior of Cr-coated Zircaloy-4 cladding tube prepared by 3D laser coating, J. Nucl. Mater. 465 (2015) 531–539. https://doi.org/10.1016/j.jnucmat.2015.06.030.

[24] J.-H. Park, H.-G. Kim, J. Park, Y.-I. Jung, D.-J. Park, Y.-H. Koo, High temperature steam-oxidation behavior of arc ion plated Cr coatings for accident tolerant fuel claddings, Surf. Coat. Technol. 280 (2015) 256–259. https://doi.org/10.1016/j.surfcoat.2015.09.022.

[25] D.J. Park, H.G. Kim, Y.I. Jung, J.H. Park, J.H. Yang, Y.H. Koo, Behavior of an improved Zr fuel cladding with oxidation resistant coating under loss-of-coolant accident conditions, J. Nucl. Mater. 482 (2016) 75–82. https://doi.org/10.1016/j.jnucmat.2016.10.021.

[26] J. Brachet, M. Dumerval, V. Lezaud-Chaillioux, M. Le Saux, E. Rouesne, D. Hamon, S. Urvoy, T. Guilbert, Q. Houmaire, C. Cobac, G. Nony, J. Rousselot, F. Lomello, F. Schuster, H. Palancher, J. Bischoff, E. Pouillier, Behavior of Chromium Coated M5TM Claddings under LOCA Conditions, Water React. Fuel Perform. Meet. 2017, Jeju Island, South Korea, September 2017.

[27] W. Zhong, P.A. Mouche, B.J. Heuser, Response of Cr and Cr-Al coatings on Zircaloy-2 to high temperature steam, J. Nucl. Mater. 498 (2018) 137–148. https://doi.org/10.1016/j.jnucmat.2017.10.021.

[28] X. Hu, C. Dong, Q. Wang, B. Chen, H. Yang, T. Wei, R. Zhang, W. Gu, D. Chen, High-temperature oxidation of thick Cr coating prepared by arc deposition for accident tolerant fuel claddings, J. Nucl. Mater. 519 (2019) 145–156. https://doi.org/10.1016/j.jnucmat.2019.01.039.

[29] J.-C. Brachet, E. Rouesne, J. Ribis, T. Guilbert, S. Urvoy, G. Nony, C. Toffolon-Masclet, M. Le Saux, N. Chaabane, H. Palancher, A. David, J. Bischoff, J. Augereau, E. Pouillier, High temperature steam oxidation of chromium-coated zirconium-based alloys: Kinetics and process, Corros. Sci. 167 (2020) 108537. https://doi.org/10.1016/j.corsci.2020.108537.

[30] X. Han, C. Chen, Y. Tan, W. Feng, S. Peng, H. Zhang, A systematic study of the oxidation behavior of Cr coatings on Zry4 substrates in high temperature steam environment, Corros. Sci. 174 (2020) 108826. https://doi.org/10.1016/j.corsci.2020.108826.

[31] E.B. Kashkarov, D.V. Sidelev, M.S. Syrtanov, C. Tang, M. Steinbrück, Oxidation kinetics of Cr-coated zirconium alloy: Effect of coating thickness and microstructure, Corros. Sci. 175 (2020) 108883. https://doi.org/10.1016/j.corsci.2020.108883.

[32] H.-B. Ma, J. Yan, Y.-H. Zhao, T. Liu, Q.-S. Ren, Y.-H. Liao, J.-D. Zuo, G. Liu, M.-Y. Yao, Oxidation behavior of Cr-coated zirconium alloy cladding in high-temperature steam above 1200 °C, Npj Mater. Degrad. 5 (2021) 7. https://doi.org/10.1038/s41529-021-00155-8.

[33] K.A. Kane, P.I.M. Stack, P.A. Mouche, R.R. Pillai, B.A. Pint, Steam oxidation of chromium corrosion barrier coatings for sic-based accident tolerant fuel cladding, J. Nucl. Mater. 543 (2021) 152561. https://doi.org/10.1016/j.jnucmat.2020.152561.

[34] J. Bischoff, C. Delafoy, C. Vauglin, P. Barberis, C. Roubeyrie, D. Perche, D. Duthoo, F. Schuster, J.-C. Brachet, E.W. Schweitzer, K. Nimishakavi, AREVA NP's enhanced accident-tolerant fuel developments: Focus on Cr-coated M5 cladding, Nucl. Eng. Technol. 50 (2018) 223–228. https://doi.org/10.1016/j.net.2017.12.004.

[35] J.-C. Brachet, I. Idarraga-Trujillo, M.L. Flem, M.L. Saux, V. Vandenberghe, S. Urvoy, E. Rouesne, T. Guilbert, C. Toffolon-Masclet, M. Tupin, C. Phalippou, F. Lomello, F. Schuster, A. Billard, G. Velisa, C. Ducros, F. Sanchette, Early studies on Cr-Coated Zircaloy-4 as enhanced

accident tolerant nuclear fuel claddings for light water reactors, J. Nucl. Mater. 517 (2019) 268–285. https://doi.org/10.1016/j.jnucmat.2019.02.018.

[36] H. Liu, Y. Feng, Y. Yao, B. Li, R. Wang, X. Shi, P. Li, J. Shu, F. Huang, Q. Huang, F. Ge, Effect of the 345 °C and 16.5 MPa autoclave corrosion on the oxidation behavior of Cr-coated zirconium claddings in the high-temperature steam, Corros. Sci. 189 (2021) 109608. https://doi.org/10.1016/j.corsci.2021.109608.

[37] S.J. Zinkle, L.L. Snead, Designing Radiation Resistance in Materials for Fusion Energy, Annu. Rev. Mater. Res. 44 (2014) 241–267. https://doi.org/10.1146/annurev-matsci-070813-113627.

[38] A.S. Kuprin, V.A. Belous, V.N. Voyevodin, R.L. Vasilenko, V.D. Ovcharenko, G.D. Tolstolutskaya, I.E. Kopanets, I.V. Kolodiy, Irradiation resistance of vacuum arc chromium coatings for zirconium alloy fuel claddings, J. Nucl. Mater. 510 (2018) 163–167. https://doi.org/10.1016/j.jnucmat.2018.07.063.

[39] A.S. Kuprin, R.L. Vasilenko, G.D. Tolstolutskaya, V.N. Voyevodin, V.A. Belous, V.D. Ovcharenko, I.E. Kopanets, Irradiation resistance of chromium coatings for ATFC in the temperature range 300–550°C, J. Nucl. Mater. 549 (2021) 152908. https://doi.org/10.1016/j.jnucmat.2021.152908.

[40] J.-C. Brachet, M. Le Saux, V. Lezaud-Chaillioux, M. Dumerval, Q. Houmaire, F. Lomello, F. Schuster, E. Monsifrot, J. Bischoff, E. Pouillier, Behavior under LOCA conditions of Enhanced Accident Tolerant Chromium Zircaloy-4 Claddings, Top Fuel 2016, Boise, ID, September 2016.

[41] M. Dumerval, Q. Houmaire, J.C. Brachet, H. Palancher, J. Bischoff, E. Poullier, Behavior of chromium coated M5 claddings upon thermal ramp tests under internal pressure (Loss-of-Coolant Accident conditions) Top Fuel 2018, Prague, Czech Republic, September 2018.

[42] J. Hazan, A. Gauthier, E. Pouillier, K. Shirvan, Semi-integral LOCA test of cold-spray chromium coated zircaloy-4 accident tolerant fuel cladding, J. Nucl. Mater. 550 (2021) 152940. https://doi.org/10.1016/j.jnucmat.2021.152940.

[43] G. Sabol, ZIRLO™ — An Alloy Development Success, J. ASTM Int. 2 (2005) 12942. https://doi.org/10.1520/JAI12942.

[44] J.P. Foster, H.K. Yueh, R.J. Comstock, M. Limback, B. Kammenzind, S.W. Dean, ZIRLO™ Cladding Improvement, J. ASTM Int. 5 (2008) 101188. https://doi.org/10.1520/JAI101188.

[45] M.A. Snead, Y. Yan, M. Howell, J.R. Keiser, K.A. Terrani, Severe Accident Test Station Design Document, ORNL Report ORNL/TM-2015/556, Oak Ridge, TN, 2015. https://doi.org/10.2172/1252142.

[46] C.P. Massey, K.A. Terrani, S.N. Dryepondt, B.A. Pint, Cladding burst behavior of Fe-based alloys under LOCA, J. Nucl. Mater. 470 (2016) 128–138. https://doi.org/10.1016/j.jnucmat.2015.12.018.

[47] Y.F. Su, P.I.M. Stack, C.J. Stephens, K.A. Kane, S. Dryepondt, R. Pillai, B.A. Pint, B.M. Tossey, Quantifying High Temperature Corrosion, NACE Paper C2021-16805, Houston, TX, 2021.

[48] P.I.M. Stack, Size of Oxidation Feature from Image Analysis, Oak Ridge National Laboratory, 2021. https://github.com/TriplePointCat/SOFIA-CV.

[49] R. Chapman, J. Crowley, A. Longest, G. Hofmann, Zirconium Cladding Deformation in a Steam Environment with Transient Heating, Zircon. Nucl. Ind., ASTM International, West Conshohocken, PA, (1979) 393-393–16. https://doi.org/10.1520/STP36692S.

[50] D.A. Powers, R.O. Meyer, Cladding Swelling and Rupture Models for LOCA Analysis, US Nucl. Regul. Comm. NUREG-0630 (1980).

[51] N.B. Pilling, R.E. Bedworth, The Oxidation of Metals at High Temperatures, J. Inst. Met. 29 (1923), 529–591.

[52] D. Arias, J.P. Abriata, The Cr−Zr (Chromium-Zirconium) system, Bull. Alloy Phase Diagr. 7 (1986) 237–244. https://doi.org/10.1007/BF02868997.

[53] C.M. Cotell, G.J. Yurek, R.J. Hussey, D.F. Mitchell, M.J. Graham, The influence of grain-boundary segregation of Y in Cr2O3 on the oxidation of Cr metal, Oxid. Met. 34 (1990) 173–200. https://doi.org/10.1007/BF00665014.